minerals

MDPI

Article

Exploring the Potential of Granite Sawing Sludge from Cuasso Al Monte (Italy) for the Development of Aluminosilicate Gel for a Sustainable Industry

Sabrina Elettra Zafarana [1], Alessandro Achilli [2], Germana Barone [1,*], Danilo Bersani [2], Claudio Finocchiaro [1], Laura Fornasini [2], Silvia Portale [1,3] and Paolo Mazzoleni [1]

[1] Department of Biological, Geological and Environmental Sciences, University of Catania, 95129 Catania, Italy; sabrina.zafarana@phd.unict.it (S.E.Z.); claudio.finocchiaro@unict.it (C.F.); silvia.portale@phd.unict.it (S.P.); paolo.mazzoleni@unict.it (P.M.)
[2] Department of Mathematical, Physical and Computer Sciences, University of Parma, 43124 Parma, Italy; alessandro.achilli@studenti.unipr.it (A.A.); danilo.bersani@unipr.it (D.B.); laura.fornasini@unipr.it (L.F.)
[3] Department of Humanities, University of Catania, 95129 Catania, Italy
* Correspondence: germana.barone@unict.it

check for updates

Academic Editors: Carlos Hoffmann Sampaio, Chiara Coletti, Maura Fugazzotto and Laura Crespo-Lopez

Received: 13 June 2025
Revised: 3 July 2025
Accepted: 7 July 2025
Published: 9 July 2025

Citation: Zafarana, S.E.; Achilli, A.; Barone, G.; Bersani, D.; Finocchiaro, C.; Fornasini, L.; Portale, S.; Mazzoleni, P. Exploring the Potential of Granite Sawing Sludge from Cuasso Al Monte (Italy) for the Development of Aluminosilicate Gel for a Sustainable Industry. *Minerals* **2025**, *15*, 718. https://doi.org/10.3390/min15070718

Abstract

This study explores the feasibility of utilizing granite sawing sludge (FC) as a precursor to produce alkali-activated materials (AAMs). To enhance the reactivity of the system, metakaolin (MK) was added and binary mixtures were synthetized. A multidisciplinary approach, including mineralogical, chemical and mechanical analysis, was employed to assess the suitability of these precursors to produce AAMs. X-Ray diffraction (XRD) and Fourier-Transform Infrared spectroscopy (FT-IR) confirmed the occurred activation reaction with the consequent increase in the amorphous content. Raman spectroscopy was used to further explore the mineralogical composition of the consolidated specimens, helping in the detection of salts, whose formation is ascribed to secondary carbonatation processes. Morphological analysis (SEM-EDS) displayed relatively uniform microstructures for all specimens. Compressive strength tests revealed that MK rich samples achieved best values compared to FC rich formulations, which exhibited reduced strength resistance. This study highlights, for the first time, the benefits of incorporating Cuasso al Monte granite sawing sludges into alkali-activated binders. Results suggested that the incorporation of FC is recommended for both environmental and economic advantages.

Keywords: alkali-activated materials; mining waste; composite materials; upcycling

1. Introduction

In recent years, global concern about environmental issues has risen due to an increased awareness of the human impact on the planet. In this respect, the United Nations have organized numerous conferences and set different goals in order to reduce emissions of greenhouse gases, with a view to an eco-friendly future. These goals involve a more sustainable use of natural resources and the preservation of ecosystems and biodiversity [1,2]. Natural resources, which are limited and non-renewable, are widely used as building materials for the construction of infrastructures that are crucial for the development of the society and define its standard of living [3].

Despite the growing economic potential of the stone industry, this field has to deal with important challenges due to high production costs, energy and water consumption. In addition, during the cutting process of stones, an estimated 30% [4,5] up to 41% [6] of the sawn block volume turns into sludge, resulting in significant waste production. This sawing sludge results from the mixing of rock powder with refrigerating water used to cool down the sawing tools. It is usually disposed of in landfills and its grainsize, generally lower than 63 µm, includes finer particles which, if improperly managed and allowed to dry, can become airborne and lead to significant environmental problems. These latter include the dispersion of respirable dust particles (i.e., 1–10 µm) into the atmosphere, which could pose health risk (i.e., silicosis) to both humans and animals through inhalation exposure [7–9]; the reduction in the porosity and permeability of soils [10], compromising the efficiency of superficial water drainage [11]; the increase in soil alkalinity and its consequent reduction in fertility, affecting the evolution of local ecosystems [12,13]. Hence, the upcycling of such waste in the construction sector could be a smart solution to decrease the impact of landfilling activity and dust release into the environment. Moreover, taking into account that the construction industry is responsible for about 23% of global CO_2 emissions [14], using these wastes for alternative materials, would be of considerable environmental and cost benefit, especially when compared to landfilling [1,15].

Within this scenario, Alkali-Activated Materials (AAMs) provide the perfect match by balancing waste exploitation while maintaining sustainable and highly performing materials [16]. AAMs represent a class of inorganic solid materials originating from the reaction of an alkaline solution with an aluminosilicate source [17]. The latter can be both natural materials (e.g., clay; [18]) or an industrial waste material (e.g., metallurgical slags; [19]). AAMs have been demonstrated to be a reasonable alternative to conventional binders thanks to their satisfactory performances from the mechanical and chemical point of view, together with good durability and specially the possibility of involving wastes and of performing the synthesis at room temperature which results in a reduction in CO_2 emissions, energy consumption and land use [17,20–23]. Some authors have already explored the possibility of producing AAMs, starting from industrial wastes such as rock sawing sludges. For examples, Portale et al., 2023, proposed Etnean (Sicily, Italy) basalt sawing sludge to produce materials to be used for building and restoration purposes, taking advantage of the chromatic and chemical compatibility with basalt rocks, locally employed as construction materials [24]. Other researchers, instead, explored the possibility of using marble sludge as substitution of cement [25–28], or the valorisation of granite sludge as aggregates for the ceramic and cement industries [15,29,30]. The application in the restoration field was also recently explored by Portale et al. (2024), who designed promising alkali-activated binders made of different sawing sludges [31]. However, to date, very little research has focused on the valorisation of granite sludges through alkali-activated processes.

In this paper, Cuasso al Monte sawing sludge (FC) was employed for the first time to evaluate its possible use as a precursor to produce AAMs. This rock sludge originated from cutting of blocks quarried from the late-Hercynian granitic plutons, which includes white and pink medium-grained granites, mainly composed of K-feldspar, albite, quartz [32]. These rocks, commercially known as "Red Porphyry", are extensively exploited for ornamental purposes (e.g., floorings and coverings) and building elements due to its durability, esthetic properties and ease of polishing [33,34]. In this research the suitability of FC to develop AAMs was investigated through a multidisciplinary approach by means of mineralogical investigation of raw materials and synthetized binders, including mechanical characterization of the final products.

2. Materials and Methods

Cuasso al Monte sawing sludge (FC) provided by Cava Bonomi (Italy) was first dried in oven at 105 ± 5 °C for 24 h and then sieved using Φ 75 µm meshes. Its chemical composition was obtained by X-Ray Fluorescence (XRF) Spectrometer S8 Tiger (Bruker AXS, Karlsruhe, Germany).

Taking into account the crystalline nature of FC, a commercial metakaolin (MK) (ARGICAL™ M1000 provided by IMERYS, Paris, France) was added to balance the alumina content of the system and thus to enhance its chemical reactivity, promoting the polycondensation reaction in alkaline environment at room temperature [35–37].

In this study, two sets of materials with different proportions of FC and MK were prepared using alkaline solutions made up of Na_2SiO_3 (supplied by Ingessil s.r.l., Montorio, Italy; with molar ratio SiO_2/Na_2O = 3) and NaOH at different concentrations. A lower molarity of NaOH (8 M) and a higher molarity (9.9 M) with the addition of water, were used as described in Table 1. The liquid to solid ratio (L/S) was kept constant at 0.4 for both sets.

Table 1. Mix design of synthetized alkaline activated materials, including results of integrity tests after 28 days.

Sample	FC (wt.%)	MK (wt.%)	NaOH 8 M (wt.%)	Na_2SiO_3 (wt.%)	H_2O (wt.%)	Integrity Test
FC10-4.6	100	-	100	-	-	Not passed
FC10-20	100	-	20	80	-	Not passed
FC10-30	100	-	30	70	-	Not passed
FC10-40	100	-	40	60	-	Not passed
FC10-50	100	-	50	50	-	Not passed
FC10-60	100	-	60	40	-	Not passed
FC10-70	100	-	70	30	-	Not passed
FC10-80	100	-	80	20	-	Not passed
FC5-40	50	50	40	60	-	Passed
FC6-40	60	40	40	60	-	Passed
FC7-40	70	30	40	60	-	Passed
FC8-40	80	20	40	60	-	Passed
FC9-40	90	10	40	60	-	Not passed
FC5-50	50	50	50	50	-	Not passed
FC6-50	60	40	50	50	-	Not passed
FC7-50	70	30	50	50	-	Not passed
FC8-50	80	20	50	50	-	Not passed
FC9-50	90	10	50	50	-	Not passed
FC5-60	50	50	60	40	-	Not passed
FC6-60	60	40	60	40	-	Not passed
FC7-60	70	30	60	40	-	Not passed
FC8-60	80	20	60	40	-	Not passed
FC9-60	90	10	60	40	-	Not passed
			NaOH 9.9 M (wt.%)			
FC5-1H_2O	50	50	25	50	25	Passed
FC3-1H_2O	30	70	25	50	25	Passed
FC4-1H_2O	40	60	25	50	25	Passed
FC4-1.5H_2O	40	60	22.2	44.4	33.3	Not passed

The powdered precursors (FC and MK) were first mixed in a mortar using a pestle, in order to obtain a homogeneous mixture. The latter was blended with the alkaline reagents. The slurry was poured into a 2 × 2 × 2 cubic mould and manually vibrated to remove any trapped air bubbles. The specimens were sealed at 25 °C (±5) for 24 h to avoid the rapid evaporation of the solution and then demoulded and cured for 28 days at room temperature.

Specimens were labelled according to their specific formulation: the first number refers to the FC content of the powder ratio divided by 10 (i.e., if the FC content is 100%, the number will be 10), while the number after the dash is the NaOH content. For the formulation with the addition of water, the ratio between water and NaOH was reported.

The chemical stability was qualitatively estimated by means of the integrity test [38], a useful preliminary procedure conducted after 28 days of curing by placing the specimens in a solution made up of deionised water, with a 1:10 (in weight) solid to liquid ratio. After 24 h, the samples are removed from the water solution and their consistency is assessed through the use of a scalpel. Moreover, the possible presence of residual debris and turbid water was also taken into account, since they are indicative of samples' chemical instability. Only the formulations that successfully performed the integrity test, namely those formulations which did not experience any loss of physical integrity, were employed for further characterizations.

Crystalline and amorphous phase identification was performed by means of X-Ray powder diffraction (XRPD), using a Miniflex diffractometer (Rigaku, Japan) (CuKα radiation, 40 kV-15 mA, step size 0.01°, scanning speed of 5°/min, $2\theta = 4°$ to 75°). Quantitative analysis was also performed to assess the crystalline and amorphous quantity, by using zincite (ZnO) as the internal standard. Profex software (Version 5.2.4) and BGMN database were then used for the elaboration of the acquired diffractograms [39].

The mineralogical composition was further investigated by Raman spectroscopy. Analyses were carried out using a Jobin Yvon LabRam spectrometer (HORIBA Scientific, Kyoto, Japan) (laser He-Ne at 632.8 nm) with 2 cm^{-1} spectra resolution, using Olympus microscope (Olympus, Tokyo, Japan) with 10× and Ultra-long working distance (ULWD) 50× and 100× objectives. Spectra were processed by using LabSpec (Version 5.58.25).

In order to assess the occurred polycondensation reaction, Fourier Transformed Infrared Spectroscopy (FT-IR) analysis was performed by using Cary 630(R) spectrometer (Agilent, Santa Clara, CA, USA). The spectra were acquired with Agilent MicroLab Software (version 5.6) within a range of 4000 to 700 cm^{-1} and a resolution of 4 cm^{-1}.

Scanning Electron Microscopy associated with Energy-Dispersion Spectroscopy (SEM-EDS) analysis were carried out in order to assess the occurrence of any differences in the microstructural features (i.e., texture, porosity and presence of relict grains) between the specimens. Specifically, a Vega-LMU scanning electron microscope (Tescan, Brno, Czech Republic) was used on carbon-coated samples, with voltage set at 20 kV and a beam current of 8 nA. Finally, the Compressive Strength tests carried were conducted to explore the mechanical performances of the samples. A UNIFRAME universal testing machine (Controls, Milan, Italy) with a 50 kN load cell was used to measure the uniaxial compressive strength of 4 specimens for each formulation. The peak sensitivity of the instrument was set at 3 kN and a test speed of 1200 N/s. The instrument sensitivity is 0.001 kN.

3. Results and Discussion

The chemical composition of the raw materials used in this research is reported in Table 2. FC showed a predominant siliceous composition, with a high SiO_2 content (i.e., 77 ± 0.4 wt.%) and moderate levels of Al_2O_3 (i.e., 12.9 ± 0.8 wt.%). It also contains considerable amounts of K_2O and Na_2O (8.7 ± 0.4 wt.%). Furthermore, minor contributions of Fe_2O_3 (1.3 ± 0.1 wt.%), CaO and MgO (0.74 ± 0.05 wt.%) were observed. The chemical composition of MK showed abundance in SiO_2 (specifically 55 wt.%) and a higher amount of Al_2O_3 (40 wt.%). The lower levels of CaO and MgO, and alkali metals (i.e., 0.3 and 0.8, respectively) confirmed its purity and suitability as an aluminosilicate precursor [17,21,40,41].

Table 2. Chemical analysis of the raw precursors obtained by X-Ray Fluorescence (XRF). Oxides are expressed in wt.%.

Sample	Al_2O_3	SiO_2	CaO + MgO	$Na_2O + K_2O$	Fe_2O_3	TiO_2
FC	12.9 ± 0.8	76.36 ± 0.4	0.74 ± 0.05	8.7 ± 0.4	1.3 ± 0.1	-
MK	35 ± 3.0	61 ± 1.7	0.26 ± 0.06	0.56 ± 0.04	1.3 ± 0.1	1.7 ± 0.2

The combination of FC and MK in different proportions allows for tailored AAM formulations, where the metakaolin contributes to the formation of a matrix though the polycondensation reaction, while the granite sludge acts as a filler and secondary source of silica, influencing the final microstructure and properties [42,43]. Further characterizations methods were performed only on specimens which successfully passed the integrity test.

3.1. Mineralogical and Molecular Characterization

Figure 1a,b showed the diffractometric patterns of the analyzed raw materials and consolidated samples. FC is mainly characterized by quartz (SiO_2), plagioclase (consisting of a solid solution between two endmembers, namely anorthite ($CaAl_2Si_2O_8$) and albite ($NaAlSi_3O_8$)), microcline ($KAlSi_3O_8$), white and black micas (i.e., muscovite ($KAl_2(AlSi_3O_{10})(OH)_2$) and biotite ($K(Mg, Fe^{2+})_3AlSi_3O_{10}(OH)_2$), respectively). In addition, the patterns showed the presence of hematite (Fe_2O_3), probably due to the interaction between water and the metallic parts of the saw during the cutting process of the rock. The displayed composition is typically reported for granite stones as well as Cuasso al Monte granophyre [32]. Moreover, quartz, muscovite and anatase (TiO_2) were identified in raw metakaolin (Figure 1a). The presence of zincite in all XRD patterns is due to the internal standard used for quantitative measurements.

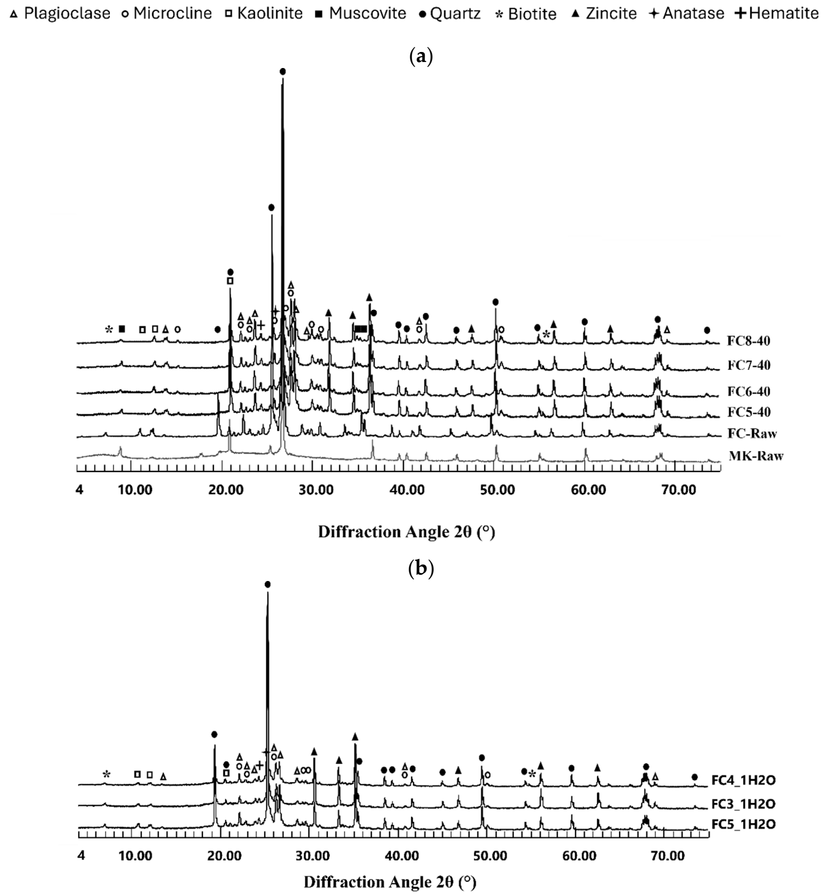

Figure 1. (**a**,**b**) X-Ray Diffraction patterns of raw and activated materials.

Consolidated materials (Figure 1a,b) showed a pattern composed of the same minerals found in the precursors. Despite the differences in precursors' proportions and concentration of the activating solutions, no remarkable differences were observed in the diffractograms [44–46].

Furthermore, a shift in the broad amorphous hump can be observed, with raw MK showing a hump centred around 23° 2θ, while the consolidated materials displayed a shift towards higher diffraction angles (i.e., ~28° 2θ). This variation is consistent with the structural transformation occurring during alkali activation, where Si-O-Si bonds are progressively replaced by Si-O-Al bonds in the forming aluminosilicate gel network [44,45].

In order to assess the occurred polycondensation reaction by the formation of N-(A)-S-H and C-(A)-S-H amorphous gel [46,47], the amount of mineralogical and amorphous phases was quantified, and it is reported in Table 3. A clear correlation between the amorphous content and the relative percentage of metakaolin in the formulation can be observed, as previously stated [48–51].

Table 3. Quantified amorphous and mineralogical phases (wt.%) for raw materials and consolidated specimens. Standard deviation was always below 0.01.

Phase [wt.%]	FC-Raw	MK-Raw	FC5-40	FC6-40	FC7-40	FC8-40	FC5-1H_2O	FC3-1H_2O	FC4-1H_2O
Amorphous	0.00	76.80	34.13	31.33	24.97	25.88	42.24	61.94	53.20
Plagioclase	17.96	1.49	18.16	15.14	14.16	14.85	8.22	12.25	11.13
Microcline	35.69	0.44	13.28	17.98	21.80	22.08	14.92	4.9	8.62
Kaolinite	-	2.88	2.81	3.05	2.51	2.26	2.95	1.9	1.98
Muscovite	1.24	1.67	1.69	0.94	1.03	1.70	0.64	1.13	1.15
Quartz	42.71	14.46	28.80	30.39	33.86	32.06	29.88	16.95	23.22
Biotite	1.49	1.49	0.59	0.27	0.9	0.35	0.41	0.30	0.36
Anatase	-	0.77	0.34	0.63	0.64	0.61	0.70	0.45	0.21
Hematite	0.91	-	0.18	0.26	0.13	0.19	0.04	0.18	0.13

In detail, all specimens showed an increase in the amorphous amount if compared to the raw FC precursor. Specifically, for specimens activated with 8 M NaOH, the amorphous amount seems to be proportionally related to the metakaolin amount. In fact, FC5-40 showed the highest value (i.e., 34.13%) while similar lowest values were obtained when both 30% and 20% of metakaolin were added (i.e., 24.97 and 25.88, respectively). This is due to the known high reactivity of metakaolin, induced by the amorphous structure which facilitates the polycondensation reaction [52]. With regards to the materials activated with 9.9 M NaOH, once again the same trend can be observed: the highest value was obtained for the sample FC3-1H_2O, which contained the highest amount of metakaolin within the set.

This finding further supports the occurrence of a polycondensation reaction. Moreover, the marked reduction in quartz, microcline and plagioclase contents for the specimens activated with 9 M NaOH, compared to the raw materials, confirmed the ability of higher molarity solutions to partially dissolve the aluminosilicate minerals grains [53].

These results highlighted the critical role of precursor proportions and NaOH molarity in tailoring the amorphous phase content and the final properties of the consolidated materials, providing hints on how to optimize the formulation of alkali-activated materials.

Micro-Raman investigations were carried out to have a more complete understanding of the species and their distribution in the samples. Internal and external parts of the specimens were analyzed, observing a uniform mineral composition. In all samples, the main phases detected are feldspar and quartz. In addition, Ca, Fe and Mg carbonates have been detected as secondary phases. No differences were observed between the various formulations and the same phases were detected uniformly both on external and internal zones.

Figure 2 shows the main peaks of feldspars recognized at 507 (I_a), 475 (I_b), 286 (II_{max}), and 151 (III_{max}) cm^{-1}, together with minor peaks detected at 403, 756 and 808 cm^{-1}. Moreover, for the position of the main peak related to the plagioclase series, applying the formula proposed by Bersani [54], it was possible to infer the contribution of anorthite and albite in the solid solution. In particular, for Δ_{ab} = 32.4 and w_a = 18.57, the presence of anorthite and albite can be stated as 47% and 53%, respectively. Furthermore, considering Δ_{ab}, the presence of some potassium ions in the structure (i.e., a ternary composition) cannot be excluded [55]. The contribution of quartz (i.e., strong peak at 466 cm^{-1} and secondary peaks at 127, 206, 264, 354 and 395 cm^{-1}) and anatase (i.e., 150 and 637 cm^{-1}) can be observed [56–60].

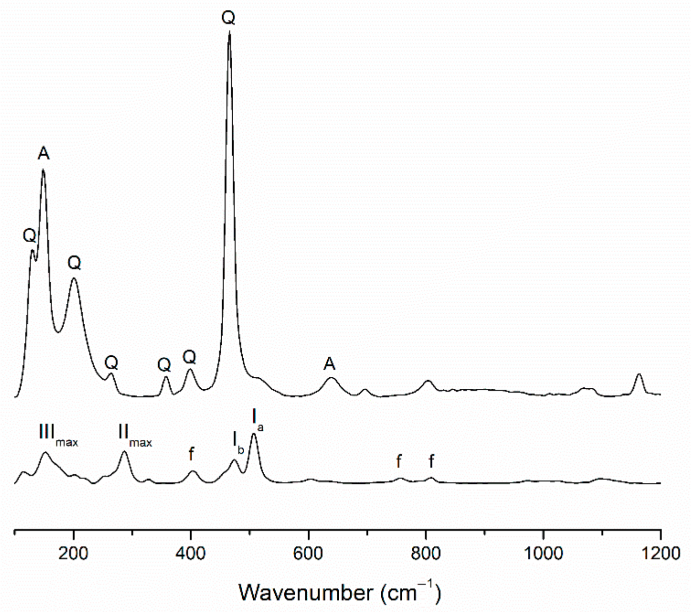

Figure 2. Raman spectra of consolidated specimens showing the presence of quartz (Q), anatase (A) and feldspar (f).

Moreover, Raman analysis, thanks to its high accuracy and non-destructivity, can be useful to identify some minor phases such as efflorescence salts forming on the activated materials. The presence of salts, mainly consisting of trona ($Na_2CO_3 \cdot NaHCO_3 \cdot 2H_2O$), gaylussite ($Na_2Ca(CO_3)_2 \cdot 5H_2O$)/pirssonite ($Na_2Ca(CO_3)_2 \cdot 2H_2O$), and natrite ($Na_2CO_3$), was detected, as stated in Figure 3. Trona was found at 1425 cm^{-1} while gaylussite/pirssonite, which is characterized by a strongest peak ranging between 1075 and 1077 cm^{-1}, was associated with a weak signal at ~1760 cm^{-1}. Gaylussite and pirssonite are very similar compounds and their peaks are characterized by slight differences in position, so it was impossible to distinguish one from the other. Therefore, both were considered together. These minerals were detected only on the samples' surface, due the carbonatation of alkaline ions coming from the solution. Moreover, hematite (i.e., peaks at 290, 402 and 606 cm^{-1}) was also observed [61–63].

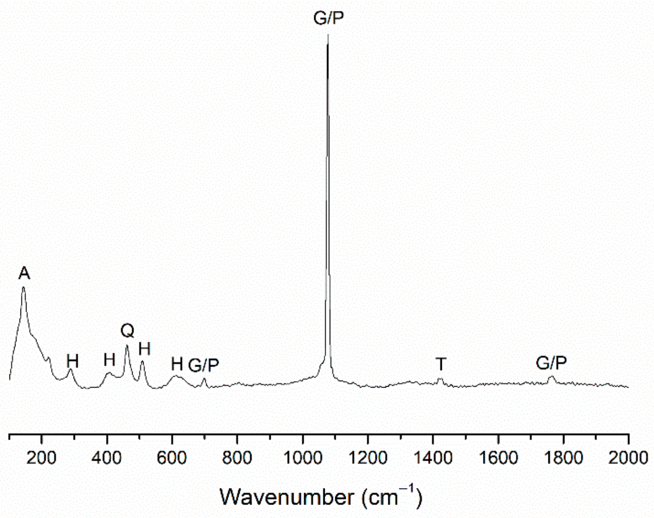

Figure 3. Raman spectra of consolidated specimens showing the presence of anatase (A), hematite (H), quartz (Q), gaylussite and pirssonite (G/P), and trona (T).

The presence of amorphous phases was not detected by micro-Raman analyses, probably due to the submicrometric size of the amorphous regions, whose signals could be covered by those related to the coexisting crystalline phases [64]. However, quantitative XRPD analysis confirmed the presence of amorphous phases, demonstrating the effectiveness of the activation process. Thus, it can be inferred that alkaline activation has primarily affected the grain boundaries of the precursors.

The results further demonstrated the potential of using Micro-Raman spectroscopy for non-destructive characterization of the mineralogical phases that made up the consolidated materials, as already proven in previous studies [64–66]. A uniform distribution of feldspars, quartz, anatase and hematite was observed, confirming a good preparation process of the activated materials. Secondary carbonate phases forming efflorescence salts, due to carbonatation processes, were noted on the material surfaces. Even though the amorphous content was not directly observed, its submicrometric presence is assumed.

Figure 4a,b displays some differences between the FT-IR spectra of the raw powdered precursors and consolidated materials. In detail, the peak located at 3364–3369 cm^{-1} is mostly attributed to O-H stretching of the aluminosilicate matrix [67]. Asymmetric stretching of O-H and bending of H-O-H molecules, due to atmospheric water absorption, was detected at 1647 cm^{-1} [68,69]. Peaks centred at 1438, and 1389 cm^{-1} are related to the presence of carbonate compounds. In particular, O-C-O stretching was likely related to the carbonation reaction between atmosphere and the exceeding sodium content in the activated material, leading to the formation of CO_3^{2-} [37,70].

The complex band ranging from 1200 to 900 cm^{-1} is ascribed to Si-O-Si and Al-O-Si vibrations [68]. In the precursors, the peaks are found at 1000, 1040 and 1087 cm^{-1}, while a shift towards lower wavenumbers is visible in the activated materials (i.e., 992 and 986 cm^{-1}). The shift to lower wavenumbers has been proven to be of significant interest for the study of the polycondensation reaction as it involves the transformation of Si-O-Si into Si-O-Al bonds of polysialate [70–74]. Hence, this may be considered as further evidence of the condensation reaction occurring and the development of a gel network. Peaks located at 795–797 cm^{-1} can be due to the presence of quartz or to Si-O-H vibration [68,69]. Moreover, Al-O and Al-OH bonds' contribution can be seen at 776/775 and 718/722 cm^{-1}, respectively [69,75].

FT-IR spectra provided a remarkable insight to the structural changes occurring after the activation of the raw materials compared to the consolidated materials. A considerable shift in Si-O-Si and Al-O-Si vibrations towards lower wavenumbers was observed, suggesting the polycondensation reaction occurred and the development of a gel network.

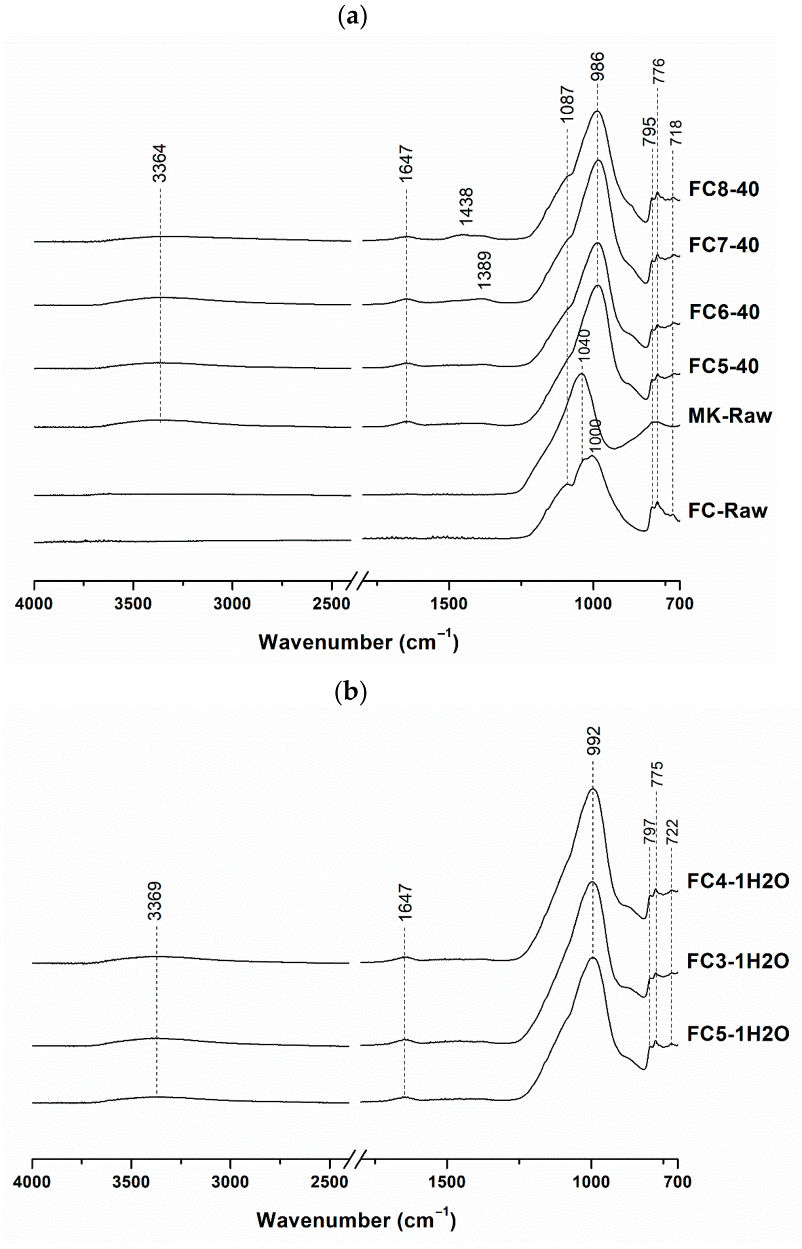

Figure 4. FT-IR spectra of raw materials and 8 M-activated specimens (**a**); 9.9 M-activated specimens (**b**).

3.2. *Morphological and Mechanical Characterization*

3.2.1. Scanning Electron Microscopy and Energy-Dispersion Spectroscopy (SEM-EDS)

Figures 5 and 6 display the SEM micrographs, with the red circles indicating the spots where the EDS analysis were performed. Spots were chosen according to their morphology, which appeared to match to amorphous regions, suggesting the likely occurrence of the aluminosilicate gel network. Specifically, Figure 5a–d show the SEM image of the sample set without the addition of water. Specimen FC5-40 exhibited a relatively uniform and dense matrix with the presence of a big unreacted grain (see the arrow in Figure 5a). Instead, the specimen FC6-40 displayed a slightly denser and uniform microstructure without any relict particles in the observed area (Figure 5b). This may be ascribed to a more effective activation reaction with the resulting formation of a well-formed aluminosilicate network. However, the absence of relict grains could also be attributed to local variability in the distribution of the particles within the specimen. Figure 5c,d reveals a very similar microstructure of the specimens FC7-40 and FC8-40. In particular, Figure 5c displays the presence of large areas of agglomerate unreacted relict minerals surrounded by uniform matrix, marked by the arrow. Some of these minerals even showed a foliated texture suggesting their possible affiliation to the mica group, detected in both FC and MK. Moreover, Figure 5d shows the presence of efflorescence, with a typical fibrous structure, marked by the arrow. For all specimens, no pores were observed at this magnification.

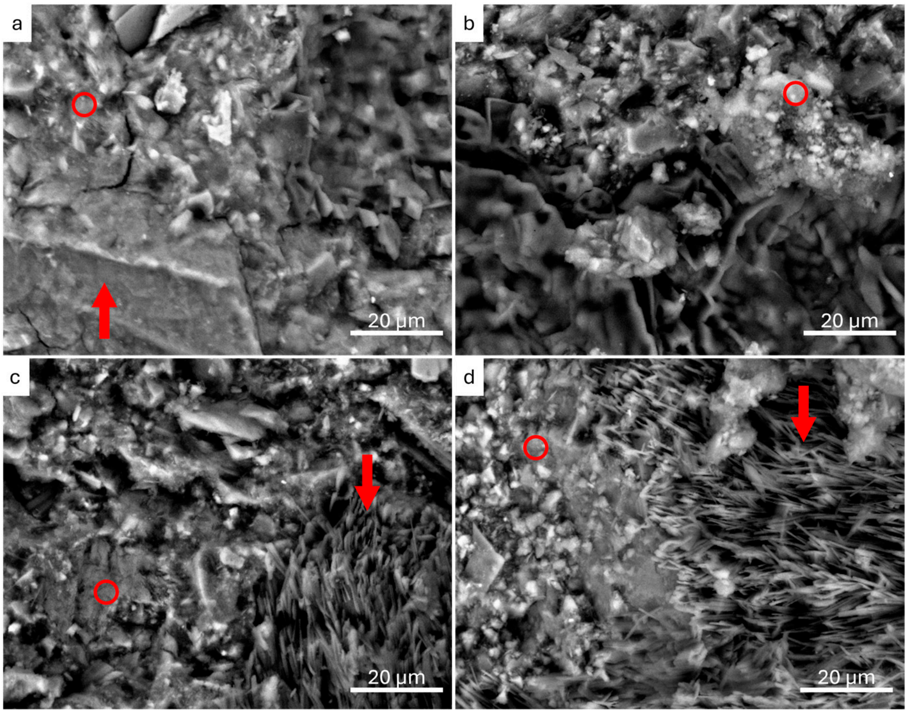

Figure 5. SEM micrographs of specimens FC5-40 (**a**), FC6-40 (**b**), FC7-40 (**c**) and FC8-40 (**d**). The red circles indicate the EDS analysis points for each specimen; red arrows show unreacted minerals and efflorescence (**a**,**c**,**d**).

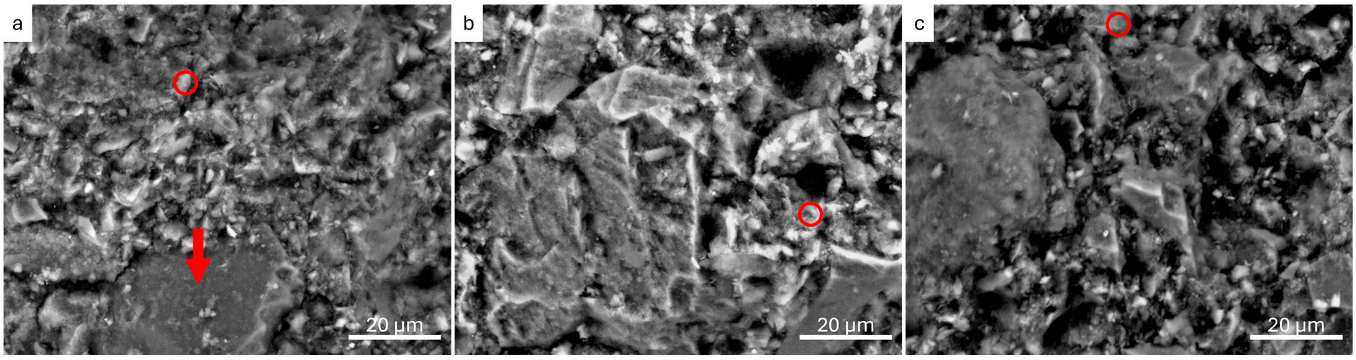

Figure 6. SEM micrographs of specimens FC5-1H_2O (**a**), FC3-1H_2O (**b**) and FC4-1H_2O (**c**). The red circles denote the EDS analysis points for each of the specimens; red arrow points out unreacted minerals.

Figure 6a–c represents the microstructure of specimens with the addition of water. Specimen FC5-1H_2O (a) highlighted a uniform microstructure with the presence of a large angular unreacted particle such as those in Figure 5a, pointed out by the arrow, probably ascribable to quartz or feldspar from the FC precursor, surrounded by the matrix. These unreacted particles do not take part in the activation reaction and seem to have limited bonding with the surrounding matrix, suggesting areas of weakness, which may lead to reduced mechanical properties. Figure 6b,c represented the micrographs of FC3-1H_2O and FC4-1H_2O, respectively, this latter exhibiting the most uniform matrix among the 3 compared specimens. Some unreacted particles are still visible but seem to be smaller in size and more embedded in the gel which appeared to be denser, suggesting a better activation of the precursors. Overall, SEM analysis displayed the existence of a more uniform and denser aluminosilicate gel when more metakaolin was used in the formulation, supporting its role as an enhancer of the activation reaction. On the contrary, the higher number of relict grains in FC-rich specimens can be statistically associated with the greater proportion of FC precursor. Moreover, the concentration of the alkaline solution is already known to have an influence on the dissolution and the activation rate of the precursors, resulting in a more compact microstructure [50,53].

Table 4 displays the elemental chemical analysis, expressed in weight percent (wt.%), performed by EDS on the points represented by the red circles shown in Figures 5 and 6. The spot analysis reveals significant variations in the elemental composition of the alkali-activated materials, directly correlated with the precursor ratios and the chemical composition of FC and MK. Samples with higher MK content (e.g., FC4-1H_2O) exhibit elevated Al content (34.8 wt.%), promoting better aluminosilicate gel formation. No trend can be detected for Na contents, whose contribution can be associated with the activator. The presence of high K abundances observed in some samples is consistent with the quantitative XRD analysis, where the percentage of microcline (K-feldspar) is also high. On the other hand, the decreased K content in specimens with added water may be due to the enhanced dissolution of microcline promoted by the 9 M NaOH solution. These results underline the importance of precursor optimization in tailoring the microstructure and properties of alkali-activated materials.

Table 4. Chemical characterization of the specimens by Energy-Dispersive Spectroscopy (EDS) analysis. Values are expressed in weight percent of the elements.

Sample	**wt.%**										
	Na	**Si**	**Al**	**Si/Al**	**Mg**	**P**	**K**	**Ca**	**Ti**	**Mn**	**Fe**
FC5-40	6.1	62.8	25.9	2.42	0.2	0.3	2.1	0.5	0.6	0.2	1.3
FC6-40	4.4	61.7	19.5	3.16	0.1	0.05	13.3	0.3	0.2	0.07	0.4
FC7-40	4.5	64	19.3	3.31	0.1	0.4	11.5	0	0	0	0.2
FC8-40	3.3	58.2	13.7	4.24	0.2	0.1	21.4	0.6	0.7	0.3	1.5
FC5-1H_2O	8.1	74	15.5	4.77	0.2	0	1.1	0.1	0.2	0.08	0.7
FC3-1H_2O	3.1	80.1	14.7	5.44	0.2	0.05	0.6	0.1	0.4	0.09	0.7
FC4-1H_2O	4.6	56	34.8	1.60	0.3	0.2	1.1	0.3	1.1	0	1.6

Finally, SEM and EDS analyses provided crucial insights into the microstructural and compositional changes in the activated materials, pointing out the critical influence of raw material ratios on gel formation and matrix uniformity.

3.2.2. Mechanical Characterization

The compressive strength values highlight the critical role of precursor ratios and activator concentrations in determining the mechanical performance of alkali-activated materials (Table 5). Specimens with higher metakaolin content, such as FC5-40 and FC6-40, exhibit the highest strength (~30 MPa), generally attributed to the formation of a more compact aluminosilicate matrix. Specimen FC6-40 reached the highest compressive resistance despite having slightly lower amorphous content than FC5-40 (i.e., 31.3% and 34.1%, respectively). This evidence suggests that the amorphous content alone does not fully explain the observed mechanical performances. Indeed, the microstructure and the amorphous phase distribution have an influence, as confirmed by SEM analysis of FC6-40, which revealed a denser and more homogeneous matrix with fewer visible unreacted particles compared to the one of FC5-40. This structural difference is most likely responsible for the improved mechanical properties. As the FC content increases (i.e., FC7-40 and FC8-40), lower mechanical performance was achieved (~20 MPa). This behaviour is due to the FC contribution, which is largely crystalline and reduces the reactivity of the system, playing a role as filler, thus limiting the extent of the polycondensation reaction. Furthermore, the materials activated with 9.9 M NaOH (namely, FC5-1H_2O, FC3-1H_2O and FC4-1H_2O) attained similar compressive strength results compared to the sample set with 8 M NaOH, with FC3-1H_2O reaching ~25 MPa due to the increased metakaolin proportion and enhanced mineral dissolution by the stronger activator. These trends partially align with the amorphous phase content (Table 2), where higher amorphous content can be linked to the improvement of the mechanical performances [76–78]. However, the mechanical features are the results of a complex interplay between different factors such as precursors' reactivity and heterogeneity, gel morphology and distribution. The best performance achieved by FC6-40 reflects the optimal balance between the discussed factors. The compressive strengths obtained by the activated materials are similar to those obtained by AAMs based on volcanic precursors by other authors [43,79,80] and in line or even higher than the values obtained using sawing sludges coming from quartz-rich, granite and generic cutting sludges [31].

Table 5. Uniaxial compressive strength values [MPa] and standard deviation.

ID	Compressive Strength [MPa]	Standard Deviation
FC5-40	27.63	2.95
FC6-40	29.37	2.77
FC7-40	23.07	1.73
FC8-40	22.23	3.52
FC5-1H_2O	18.63	2.2
FC3-1H_2O	24.87	0.95
FC4-1H_2O	22.64	2.04

Overall, a clear relationship between precursor ratio, microstructural features, and the alkaline activator concentration was found again.

4. Conclusions

This study investigated the feasibility of using granite sawing sludge (FC) in the alkali activation process. However, its mineralogical composition has required the addition of metakaolin (MK), producing two different binary mixture-sets, whose features were determined by a multidisciplinary approach. The following key conclusions were drawn:

Although predominantly crystalline, FC may take part in the alkaline activation reaction, while MK played an essential role in enhancing the reactivity of the system, driving the formation of an aluminosilicate gel thanks to its high alumina content. This behaviour was proved by the increased amorphous phase content and the denser microstructure observed for formulations with higher MK contents.

The correlation between amorphous phase content and mechanical performance highlighted the critical role of MK in improving material properties. SEM-EDS and compressive strength tests revealed that formulations with higher MK content achieved superior mechanical properties due to better gel formation and matrix uniformity. In contrast, the FC-rich samples showed the presence of unreacted grains, which resulted in the decrease in mechanical performance.

This study demonstrated the potentiality of using waste FC as a filler in AAMs, providing a sustainable alternative to traditional binders. The combination of FC and MK not only reduces the disposal and storage of industrial waste but also produces materials with good mechanical properties. Despite the reduced reactivity induced by FC, due to its crystalline nature, its inclusion contributes to waste valorization and cost reduction. The formulation of binary mixtures composed of FC and MK represents a good compromise between mechanical performances and sustainability, allowing for a reduction in the use of natural resources and commercial precursors. This approach encourages the promotion of circular economy practices in the construction industry, while facing waste management challenges in the stone sector. However, while the results demonstrated the effectiveness of the incorporation of this material to produce AAMs, future studies should focus on the scalability of the process, which may be affected by the intrinsic chemical variability of the sludges. Moreover, durability and long-term physical-mechanical properties should be further analyzed.

Author Contributions: Conceptualization, S.E.Z., A.A., G.B., D.B., C.F., L.F., S.P. and P.M.; methodology, S.E.Z., A.A., G.B., D.B., C.F., L.F., S.P. and P.M.; formal analysis, S.E.Z., A.A., L.F. and S.P.; investigation, S.E.Z., A.A., L.F. and S.P.; resources, G.B., D.B. and P.M.; data curation, S.E.Z. and A.A.; writing—original draft preparation, S.E.Z., A.A., C.F. and S.P.; writing—review and editing, S.E.Z., G.B., D.B., C.F., S.P. and P.M.; supervision, P.M.; funding acquisition, G.B. All authors have read and agreed to the published version of the manuscript.

Funding: This research was funded by the Italian Ministry of University and Research through the PNRR PE "CHANGES—Cultural Heritage Active Innovation for Sustainable Society" (CUP E63C22001960006; PE_00000020) programme.

Data Availability Statement: The raw data supporting the conclusions of this article will be made available by the authors on request.

Acknowledgments: The authors would like to express their deep gratitude to Paolo Gentile (University of Milano Bicocca) and Renato Bonomi (owner of Bonomi quarry) for providing the raw granite sludge, and to Hana Kaňková and Lenka Buňová from the Centre for Functional and Surface Functionalized Glass (Slovakia) for performing the XRF analysis in a timely manner.

Conflicts of Interest: The authors declare no conflicts of interest.

References

1. Ramón-Álvarez, I.; Batuecas, E.; Sánchez-Delgado, S.; Torres-Carrasco, M. Mechanical performance after high-temperature exposure and Life Cycle Assessment (LCA) according to unit of stored energy of alternative mortars to Portland cement. *Constr. Build. Mater.* **2023**, *365*, 130082. [CrossRef]
2. Arora, N.K.; Mishra, I. United Nations Sustainable Development Goals 2030 and environmental sustainability: Race against time. *Environ. Sustain.* **2019**, *2*, 339–342. [CrossRef]
3. Brilha, J.; Gray, M.; Pereira, D.; Pereira, P. Geodiversity: An integrative review as a contribution to the sustainable management of the whole of nature. *Environ. Sci. Policy* **2018**, *86*, 19–28. [CrossRef]
4. Coppola, B.; Palmero, P.; Montanaro, L.; Tulliani, J.M. Alkali-activation of marble sludge: Influence of curing conditions and waste glass addition. *J. Eur. Ceram. Soc.* **2020**, *40*, 3776–3787. [CrossRef]
5. Montani, C. Congiuntura internazionale Produzione Scambi Consumi Tecnologie Beni strumentali Schede dei Paesi Leader. In *XXXII Rapporto Marmo e Pietre nel Mondo 2021 Marble and Stones in the World XXXII Report*; International Situation Production Interchange Consumption Technology Tools Profiles of Leading Countries; Aldus: Venice, Italy, 2021.
6. Jalalian, M.H.; Bagherpour, R.; Khoshouei, M. Wastes production in dimension stones industry: Resources, factors, and solutions to reduce them. *Environ. Earth Sci.* **2021**, *80*, 560. [CrossRef]

7. Mosaferi, M.; Dianat, I.; Khatibi, M.S.; Mansour, S.N.; Fahiminia, M.; Hashemi, A.A. Review of Environmental Aspects and Waste Management of Stone Cutting and Fabrication Industries. *J. Mater. Cycles Waste Manag.* **2014**, *16*, 721–730. [CrossRef]
8. Kramer, M.R.; Blanc, P.D.; Fireman, E.; Amital, A.; Guber, A.; Rhahman, N.A.; Shitrit, D. Artificial Stone Silicosis: Disease Resurgence Among Artificial Stone Workers. *Chest* **2012**, *142*, 419–424. [CrossRef]
9. Zari, M.; Smith, R.; Ferrari, R. Evaluation of Dust Emission Rate from Landfill Mining Activities. *Detritus* **2023**, *25*, 78–89. [CrossRef]
10. Sivacoumar, R.; Jayabalou, R.; Swarnalatha, S.; Balakrishnan, K. Particulate Matter from Stone Crushing Industry: Size Distribution and Health Effects. *J. Environ. Eng.* **2006**, *132*, 405–414. [CrossRef]
11. Piccini, L.; Di Lorenzo, T.; Costagliola, P.; Galassi, D.M.P. Marble Slurry's Impact on Groundwater: The Case Study of the Apuan Alps Karst Aquifers. *Water* **2019**, *11*, 2462. [CrossRef]
12. Montero, M.J.; Araque, R.A.; Rey, J.M. Occupational health and safety in the framework of corporate social responsibility. *Saf. Sci.* **2009**, *47*, 1440–1445. [CrossRef]
13. Construction & Demolition Debris Management for Sustainable Reconstruction After Disasters. Italian Case Studies. Available online: https://www.researchgate.net/publication/236648331_Construction_Demolition_debris_management_for_sustainable_reconstruction_after_disasters_Italian_case_studies (accessed on 6 April 2024).
14. Chen, J.; Wang, Y.; Shi, Q.; Peng, X.; Zheng, J. An international comparison analysis of CO_2 emissions in the construction industry. *Sustain. Dev.* **2021**, *29*, 754–767. [CrossRef]
15. Surra, E.; Sousa, J.; Correia, M.; Carvalheiras, J.; Labrincha, J.A.; Marques, J.C.; Lapa, N.; Delerue-Matos, C. Technical, Environmental, and Cost Assessment of Granite Sludge Valorisation. *Appl. Sci.* **2023**, *13*, 4513. [CrossRef]
16. Uysal, M.; Aygörmez, Y.; Canpolat, O.; Cosgun, T.; Kuranlı, Ö. Investigation of using waste marble powder, brick powder, ceramic powder, glass powder, and rice husk ash as eco-friendly aggregate in sustainable red mud-metakaolin based geopolymer composites. *Constr. Build. Mater.* **2022**, *361*, 129718. [CrossRef]
17. Provis, J.L. Alkali-activated materials. *Cem. Concr. Res.* **2018**, *114*, 40–48. [CrossRef]
18. Stroscio, A.; Barone, G.; Fernàndez-Jimenez, A.; Lancellotti, I.; Leonelli, C.; Mazzoleni, P. Sicilian clay sediments as precursor for alkali activated materials. *Appl. Clay Sci.* **2024**, *253*, 107350. [CrossRef]
19. Lancellotti, I.; Piccolo, F.; Traven, K.; Češnovar, M.; Ducman, V.; Leonelli, C. Alkali Activation of Metallurgical Slags: Reactivity, Chemical Behavior, and Environmental Assessment. *Materials* **2021**, *14*, 639. [CrossRef]
20. Bernal, S.A.; Provis, J.L. Durability of alkali-activated materials: Progress and perspectives. *J. Am. Ceram. Soc.* **2014**, *97*, 997–1008. [CrossRef]
21. Provis, J.L.; Bernal, S.A. Geopolymers and related alkali-activated materials. *Annu. Rev. Mater. Res.* **2014**, *44*, 299–327. [CrossRef]
22. Duxson, P.; Provis, J.L.; Lukey, G.C.; van Deventer, J.S.J. The role of inorganic polymer technology in the development of 'green concrete'. *Cem. Concr. Res.* **2007**, *37*, 1590–1597. [CrossRef]
23. Davidovits, J. Geopolymers: Inorganic polymeric new materials. *J. Therm. Anal. Calorim.* **1991**, *37*, 1633–1656. [CrossRef]
24. Portale, S.; Finocchiaro, C.; Occhipinti, R.; Mazzoleni, P.; Barone, G. Feasibility study about the use of basalt sawing sludge in building and restoration. *Mater. Lett.* **2023**, *333*, 133624. [CrossRef]
25. Salihoglu, N.K.; Salihoglu, G. Marble Sludge Recycling by Using Geopolymerization Technology. *J. Hazard. Toxic Radioact. Waste* **2018**, *22*, 04018019. [CrossRef]
26. Aruntaş, H.Y.; Gürü, M.; Dayı, M.; Tekin, I. Utilization of waste marble dust as an additive in cement production. *Mater. Des.* **2010**, *31*, 4039–4042. [CrossRef]
27. Corinaldesi, V.; Moriconi, G.; Naik, T.R. Characterization of marble powder for its use in mortar and concrete. *Constr. Build. Mater.* **2010**, *24*, 113–117. [CrossRef]
28. Alyamaç, K.E.; Ince, R. A preliminary concrete mix design for SCC with marble powders. *Constr. Build. Mater.* **2009**, *23*, 1201–1210. [CrossRef]
29. Lozano-Lunar, A.; Dubchenko, I.; Bashynskyi, S.; Rodero, A.; Fernández, J.M.; Jiménez, J.R. Performance of Self-Compacting Mortars with Granite Sludge as Aggregate. *Constr. Build. Mater.* **2020**, *251*, 118998. [CrossRef]
30. Zichella, L.; Dino, G.A.; Bellopede, R.; Marini, P.; Padoan, E.; Passarella, I. Environmental Impacts, Management and Potential Recovery of Residual Sludge from the Stone Industry: The Piedmont Case. *Resour. Policy* **2020**, *65*, 101562. [CrossRef]
31. Portale, S.; Mazzoleni, P.; Barone, G. Alkali activated binders based on rock sawing sludges: Synthesis, characterization and future perspectives. *Constr. Build. Mater.* **2024**, *450*, 138669. [CrossRef]
32. Gramaccioli, C.M.; Diella, V.; Demartin, F.; Orlandi, P.; Campostrini, I. Cesian Bazzite and Thortveitite from Cuasso Al Monte, Varese, Italy: A Comparison with the Material from Baveno, and Inferred Origin. *Can. Mineral.* **2000**, *38*, 1409–1418.
33. Capitani, G.; Mugnaioli, E.; Gentile, P. Submicrometer yttrian zircon coating and arborescent aeschynite microcrystals on truncated bipyramidal anatase: An electron microscopy study of miarolitic cavities in the Cuasso al Monte granophyre (Varese, Italy). *Am. Mineral.* **2023**, *103*, 480–488. [CrossRef]

34. Pezzotta, F.; Diella, V.; Guastoni, A. Scandium silicates from the Baveno and Cuasso al Monte NYF-granites, Southern Alps (Italy): Mineralogy and genetic inferences. *Am. Mineral.* **2005**, *90*, 1442–1452. [CrossRef]
35. Pacheco-Torgal, F.; Labrincha, J.; Leonelli, C.; Palomo, A.; Chindaprasirt, P. *Handbook of Alkali-Activated Cements, Mortars and Concretes*, 1st ed.; Woodhead Publishing: Sawston, UK, 2014; pp. 1–830. [CrossRef]
36. Pacheco-Torgal, F.; Castro-Gomes, J.; Jalali, S. Investigations of tungsten mine waste geopolymeric binder: Strength and microstructure. *Constr. Build. Mater.* **2008**, *22*, 2212–2219. [CrossRef]
37. Finocchiaro, C.; Barone, G.; Mazzoleni, P.; Leonelli, C.; Gharzouni, A.; Rossignol, S. FT-IR study of early stages of alkali activated materials based on pyroclastic deposits (Mt. Etna, Sicily, Italy) using two different alkaline solutions. *Constr. Build. Mater.* **2020**, *262*, 120095. [CrossRef]
38. Lancellotti, I.; Catauro, M.; Ponzoni, C.; Bollino, F.; Leonelli, C. Inorganic polymers from alkali activation of metakaolin: Effect of setting and curing on structure. *J. Solid State Chem.* **2013**, *200*, 341–348. [CrossRef]
39. BGMN Home. Available online: http://www.bgmn.de/index.html (accessed on 18 December 2024).
40. Longhi, M.A.; Rodríguez, E.D.; Walkley, B.; Eckhard, D.; Zhang, Z.; Provis, J.L.; Kirchheim, A.P. Metakaolin-based geopolymers: Efflorescence and its effect on microstructure and mechanical properties. *Ceram. Int.* **2022**, *48*, 2212–2229. [CrossRef]
41. Provis, J.L. Geopolymers and other alkali activated materials: Why, how, and what? *Mater. Struct.* **2014**, *47*, 11–25. [CrossRef]
42. Yang, J.; Xu, L.; Wu, H.; Jin, J.; Liu, L. Microstructure and mechanical properties of metakaolin-based geopolymer composites containing high volume of spodumene tailings. *Appl. Clay Sci.* **2022**, *218*, 106412. [CrossRef]
43. Palmero, P.; Formia, A.; Tulliani, J.M.; Antonaci, P. Valorisation of alumino-silicate stone muds: From wastes to source materials for innovative alkali-activated materials. *Cem. Concr. Compos.* **2017**, *83*, 251–262. [CrossRef]
44. Ghorbani, S.; Stefanini, L.; Sun, Y.; Walkley, B.; Provis, J.L.; De Schutter, G.; Matthys, S. Characterisation of alkali-activated stainless steel slag and blast-furnace slag cements. *Cem. Concr. Compos.* **2023**, *143*, 105230. [CrossRef]
45. Onutai, S.; Osugi, T.; Sone, T. Alumino-Silicate Structural Formation during Alkali-Activation of Metakaolin: In-Situ and Ex-Situ ATR-FTIR Studies. *Materials* **2023**, *16*, 985. [CrossRef]
46. Zhang, D.W.; Zhao, K.F.; Wang, D.M.; Li, H. Relationship of amorphous gel-microstructure-elastoviscosity properties of alkali-activated materials fresh pastes with different Ms waterglass. *Constr. Build. Mater.* **2021**, *287*, 123023. [CrossRef]
47. Zhang, D.W.; Zhao, K.F.; Xie, F.Z.; Li, H.; Wang, D.M. Effect of water-binding ability of amorphous gel on the rheology of geopolymer fresh pastes with the different NaOH content at the early age. *Constr. Build. Mater.* **2020**, *261*, 120529. [CrossRef]
48. Pascual, A.B.; Tognonvi, T.M.; Tagnit-Hamou, A. Optimization study of waste glass powder-based alkali activated materials incorporating metakaolin: Activation and curing conditions. *J. Clean. Prod.* **2021**, *308*, 127435. [CrossRef]
49. Bignozzi, M.C.; Manzi, S.; Lancellotti, I.; Kamseu, E.; Barbieri, L.; Leonelli, C. Mix-design and characterization of alkali activated materials based on metakaolin and ladle slag. *Appl. Clay Sci.* **2013**, *73*, 78–85. [CrossRef]
50. Kuenzel, C.; Neville, T.; Donatello, S.; Vandeperre, L.; Boccaccini, A.; Cheeseman, C. Influence of metakaolin characteristics on the mechanical properties of geopolymers. *Appl. Clay Sci.* **2013**, *83–84*, 308–314. [CrossRef]
51. Vogt, O.; Ukrainczyk, N.; Ballschmiede, C.; Koenders, E. Reactivity and Microstructure of Metakaolin Based Geopolymers: Effect of Fly Ash and Liquid/Solid Contents. *Materials* **2019**, *12*, 3485. [CrossRef]
52. Li, L.; Xie, J.; Zhang, B.; Feng, Y.; Yang, J. A state-of-the-art review on the setting behaviours of ground granulated blast furnace slag- and metakaolin-based alkali-activated materials. *Constr. Build. Mater.* **2023**, *368*, 130389. [CrossRef]
53. Pundienė, I.; Pranckevičienė, J.; Zhu, C.; Kligys, M. The role of temperature and activator solution molarity on the viscosity and hard structure formation of geopolymer pastes. *Constr. Build. Mater.* **2021**, *272*, 121661. [CrossRef]
54. Bersani, D.; Aliatis, I.; Tribaudino, M.; Mantovani, L.; Benisek, A.; Carpenter, M.A.; Gatta, G.D.; Lottici, P.P. Plagioclase composition by Raman spectroscopy. *J. Raman Spectrosc.* **2018**, *49*, 684–698. [CrossRef]
55. Freeman, J.J.; Wang, A.; Kuebler, K.E.; Jolliff, B.L.; Haskin, L.A. Characterization of Natural Feldspars by Raman Spectroscopy for Future Planetary Exploration. *Can. Mineral.* **2008**, *46*, 1477–1500. [CrossRef]
56. Jovanovski, G.; Šijakova-Ivanova, T.; Boev, I.; Boev, B.; Makreski, P. Intriguing minerals: Quartz and its polymorphic modifications. *ChemTexts* **2022**, *8*, 14. [CrossRef]
57. Krishnamurti, D. The Raman Spectrum of Quartz and Its Interpretation. *Proc. Indian Acad. Sci.* **1985**, *47*, 276–291.
58. Sato, R.K.; McMillan, P.F. An infrared and Raman study of the isotopic species of α-quartz. *J. Phys. Chem.* **1987**, *91*, 3494–3498. [CrossRef]
59. Ohsaka, T.; Izumi, F.; Fujiki, Y. Raman spectrum of anatase, TiO_2. *J. Raman Spectrosc.* **1978**, *7*, 321–324. [CrossRef]
60. Bersani, D.; Lottici, P.P.; Montenero, A. Micro-Raman investigation of iron oxide films and powders produced by sol-gel syntheses. *J. Raman Spectrosc.* **1999**, *30*, 355–360. [CrossRef]
61. Jentzsch, P.V.; Kampe, B.; Ciobotă, V.; Rösch, P.; Popp, J. Inorganic salts in atmospheric particulate matter: Raman spectroscopy as an analytical tool. *Spectrochim. Acta Part A Mol. Biomol. Spectrosc.* **2013**, *115*, 697–708. [CrossRef]
62. Frost, R.L.; Dickfos, M. Hydrated double carbonates–A Raman and infrared spectroscopic study. *Polyhedron* **2007**, *26*, 4503–4508. [CrossRef]

63. Gómez-Laserna, O.; Arrizabalaga, I.; Prieto-Taboada, N.; Olazabal, M.Á.; Arana, G.; Madariaga, J.M. In situ DRIFT, Raman, and XRF implementation in a multianalytical methodology to diagnose the impact suffered by built heritage in urban atmospheres. *Anal. Bioanal. Chem.* **2015**, *407*, 5635–5647. [CrossRef]
64. Caggiani, M.C.; Coccato, A.; Barone, G.; Finocchiaro, C.; Fugazzotto, M.; Lanzafame, G.; Occhipinti, R.; Stroscio, A.; Mazzoleni, P. Raman spectroscopy potentiality in the study of geopolymers reaction degree. *J. Raman Spectrosc.* **2022**, *53*, 617–629. [CrossRef]
65. Kosor, T.; Nakić-Alfirević, B.; Gajović, A. Geopolymerization index of fly ash geopolymers. *Vib. Spectrosc.* **2016**, *85*, 104–111. [CrossRef]
66. Mirmoghtadaei, R.; Shen, L.; Li, Y.; Li, M.; Wang, B. Enhancing alkali-activated materials with low quality fly ash: A novel mixing approach for robust construction materials. *J. Clean. Prod.* **2023**, *421*, 138261. [CrossRef]
67. Ramteke, D.D.; Hujova, M.; Kraxner, J.; Galusek, D.; Romero, A.R.; Falcone, R.; Bernardo, E. Up-cycling of ‘unrecyclable’ glasses in glass-based foams by weak alkali-activation, gel casting and low-temperature sintering. *J. Clean. Prod.* **2021**, *278*, 123985. [CrossRef]
68. Ben Messaoud, I.; Hamdi, N.; Srasra, E.; Lavorgna, M. Physicochemical Characterization of Geopolymer Binders and Foams Made from Tunisian Clay. *Adv. Mater. Sci. Eng.* **2018**, *2018*, 9392743. [CrossRef]
69. Yusan, S.; Bampaiti, A.; Aytas, S.; Erenturk, S.; Aslani, M.A.A. Synthesis and structural properties of ZnO and diatomite-supported ZnO nanostructures. *Ceram. Int.* **2016**, *42*, 2158–2163. [CrossRef]
70. Azhar, N.S.D.M.; Zainal, F.F.; Abdullah, M.M.A.B. Bonding and Phases Analysis of Geopolymer Materials. In Proceedings of the IOP Conference Series: Materials Science and Engineering, International Conference on Sustainable Materials (ICoSM 2020), Pahang, Malaysia, 30 March 2020; Volume 957, p. 012052. [CrossRef]
71. Khan, M.I.; Azizli, K.; Sufian, S.; Siyal, A.A.; Man, Z. Sodium Silicate Free Geopolymer as Coating Material: Adhesion to Steel. In Proceedings of the 1st International Electronic Conference on Materials, Online, 26 May–10 June 2014. [CrossRef]
72. Rees, C.A.; Provis, J.L.; Lukey, G.C.; van Deventer, J.S.J. In situ ATR-FTIR study of the early stages of fly ash geopolymer gel formation. *Langmuir* **2007**, *23*, 9076–9082. [CrossRef] [PubMed]
73. Rees, C.A.; Provis, J.L.; Lukey, G.C.; van Deventer, J.S.J. Attenuated total reflectance fourier transform infrared analysis of fly ash geopolymer gel aging. *Langmuir* **2007**, *23*, 8170–8179. [CrossRef]
74. Hajimohammadi, A.; Provis, J.L.; van Deventer, J.S.J. Time-resolved and spatially-resolved infrared spectroscopic observation of seeded nucleation controlling geopolymer gel formation. *J. Colloid Interface Sci.* **2011**, *357*, 384–392. [CrossRef]
75. Christophliemk, M.; Pikkarainen, A.; Heponiemi, A.; Tuomikoski, S.; Runtti, H.; Hu, T.; Kantola, A.; Lassi, U. Preparation and characterization of porous and stable sodium- and potassium-based alkali activated material (AAM). *Appl. Clay Sci.* **2022**, *230*, 106697. [CrossRef]
76. Shariati, M.; Shariati, A.; Trung, N.T.; Shoaei, P.; Ameri, F.; Bahrami, N.; Zamanabadi, S.N. Alkali-activated slag (AAS) paste: Correlation between durability and microstructural characteristics. *Constr. Build. Mater.* **2021**, *267*, 120886. [CrossRef]
77. Duxson, P.; Provis, J.L.; Lukey, G.C.; Mallicoat, S.W.; Kriven, W.M.; van Deventer, J.S.J. Understanding the relationship between geopolymer composition, microstructure and mechanical properties. *Colloids Surf. A Physicochem. Eng. Asp.* **2005**, *269*, 47–58. [CrossRef]
78. Davidovits, J. Geopolymers: Ceramic-like inorganic polymers. *J. Ceram. Sci. Technol.* **2017**, *8*, 335–350. [CrossRef]
79. Occhipinti, R.; Caggiani, M.C.; de Ferri, L.; Xu, Z.; Steindal, C.C.; Razavi, N.; Andriulo, F.; Mazzoleni, P.; Barone, G. Structural properties of volcanic precursors-based geopolymers before and after natural weathering. *Ceram. Int.* **2023**, *49*, 21892–21902. [CrossRef]
80. Finocchiaro, C.; Barone, G.; Mazzoleni, P.; Cultrone, G. Insight on physical–mechanical properties of one-part alkali-activated materials based on volcanic deposits of Mt. Etna (Italy) and their durability against ageing tests. *Mater. Struct.* **2024**, *57*, 198. [CrossRef]